

**Notice:** This manuscript has been authored by UT-Battelle, LLC, under Contract No. DE-AC0500OR22725 with the U.S. Department of Energy. The United States Government retains and the publisher, by accepting the article for publication, acknowledges that the United States Government retains a non-exclusive, paid-up, irrevocable, world-wide license to publish or reproduce the published form of this manuscript, or allow others to do so, for the United States Government purposes. The Department of Energy will provide public access to these results of federally sponsored research in accordance with the DOE Public Access Plan (<http://energy.gov/downloads/doe-public-access-plan>).

# Physics discovery in nanoplasmonic systems *via* autonomous experiments in Scanning Transmission Electron Microscopy

Kevin Roccapiore,<sup>1</sup> Sergei V. Kalinin,<sup>1,a</sup> and Maxim Ziatdinov<sup>1,2,b</sup>

<sup>1</sup> Center for Nanophase Materials Sciences, Oak Ridge National Laboratory, Oak Ridge, TN, USA, 37831

<sup>2</sup> Computational Sciences and Engineering Division, Oak Ridge National Laboratory, Oak Ridge, TN, USA, 37831

Physics-driven discovery in an autonomous experiment has emerged as a dream application of machine learning in physical sciences. Here we develop and experimentally implement deep kernel learning workflow combining the correlative prediction of the target functional response and its uncertainty from the structure, and physics-based selection of acquisition function guiding the navigation of the image space. Compared to classical Bayesian optimization methods, this approach allows to capture the complex spatial features present in the images of realistic materials, and dynamically learn structure-property relationships towards physical discovery. Here, this approach is illustrated for nanoplasmonic studies of the nanoparticles and experimentally implemented for bulk- and edge plasmon discovery in MnPS<sub>3</sub>, a lesser-known beam-sensitive layered 2D material. This approach is universal and is expected to be applicable to probe-based microscopic techniques including other STEM modalities and Scanning Probe Microscopies.

---

<sup>a</sup> sergei2@ornl.gov

<sup>b</sup> ziatdinovma@ornl.gov

The emergence of advanced electron and scanning probe microscopies has opened fundamentally new opportunities for exploring the physics of nanoscale and atomic systems.<sup>1–3</sup> Over the last decades, multiple advances ranging from mapping structure of ferroic<sup>4,5</sup> and charge density wave systems,<sup>6,7</sup> to exploring the nature of electronic and superconductive order parameters in quantum materials,<sup>8,9</sup> to probing vibrational and plasmonic properties on the nanometer and atomic level<sup>10–12</sup> has become commonplace. The advent of monochromated and aberration-corrected electron microscopy<sup>13</sup> combined with the beam engineering<sup>14</sup> and low-temperature environments<sup>15</sup> opens the pathway towards further advancements.

In scanning transmission electron microscopy (STEM), one of the most prominent recent experimental directions is the high-energy resolution low-loss electron energy loss spectroscopy (EELS) for probing phononic and plasmonic properties.<sup>16,17</sup> These responses contain the information on the local dielectric function convolved with local geometry,<sup>18–20</sup> and hence contain the key to understanding the physics of collective excitations in the nanoscale systems. Similarly, plasmons strongly couple to local chemical reactivity and form the basis for chemical characterization or even beam-controlled chemical reactions. Finally, the development of multiple classes of quantum devices hinges on the capability to understand and harness phonon and plasmon functionalities on the nanometer levels.

These considerations have stimulated the large body of experimental effort in EEL spectroscopy and EELS imaging of 2D materials, nano-optical systems, semiconductors, and many more.<sup>21,22,13</sup> Currently, the experimental studies in STEM-EELS, much like virtually all other areas of modern physical imaging, are based on the human operator paradigm. The regions for spectral imaging, whether single point spectroscopy or a grid of points, are selected based on operator intuition, and data analysis is performed after (in some cases, long after) it has been acquired. At the same time, generative theoretical models for many of these are poorly understood, have a large number of poorly known parameters, or are absent. Hence, experimental discovery of new physical relationships and behaviors is often limited by chance, i.e., whether the object or behaviors of interest happened to be observed during the experiment and if they contain features identifiable by an operator and collaborating team. Note that multiple calls for storing full experimental data streams and making the data open that are now prevalent in multiple scientific communities<sup>23,24</sup> seek to address the second aspect.

These considerations have launched much interest in automated and autonomous experiment as an approach to accelerate the rate of physical discovery. Over the last several years, multiple opinion pieces towards development of AE in microscopy have been published.<sup>25,26</sup> However, the targets of the automated experiment have not been generally analyzed in detail, with vast majority of applications to date reporting either probe-based manipulation based on rigid discovery and manipulation rules,<sup>27,28</sup> or implementation of deep neural network-based computer vision algorithms towards identification of objects of interest over large scan regions.<sup>29–31</sup> At the same time, automated discovery of novel physical phenomena has remained elusive. Currently, the primary bottleneck towards implementation of the autonomous experiment in microscopy is the lack of the algorithm for active learning targeting *physical* discovery.

Indeed, in many areas of scientific research including X-Ray scattering, automated synthesis, and recently SPM and STEM, the primary paradigm for the AE is Gaussian Processes (GP) and GP-based Bayesian optimization (BO).<sup>32–35</sup> However, the extant implementations of BO use only the information acquired during the experiment to select the new locations for exploration. Similarly, the relationship between the explored locations is defined by the functional form of the kernel function (somewhat equivalent to the parametrized correlation function discovered during the experiment), thus offering only limited flexibility. While new forms of kernel functions are becoming available and the non-parametric and analytic forms of acquisition functions can be balanced, the lack of prior knowledge utilization is common to the BO methods that are also usually limited to low-dimensional parameter space. Secondly, the learning of kernel structure is effectively equivalent to the discovery of correlation function parametrized *via* a certain functional form, and hence their capability to represent complex non-periodic spatial structures prevalent in microscopic data is extremely limited.

At the same time, in the typical microscopy experiment, the locations for the detailed spectroscopic or imaging studies is selected based on specific features in the structural data set. For example, in nanoplasmonic structures we want to collect EEL spectra on “special” locations associated with certain positions with respect to geometric structures. This information is not available for conventional BO. Ideally, we would like to balance this feature-based exploration with the perceived value of the already-discovered behaviors, for example, intensities in a specific energy region, functional form of the spectrum, presence of features that are expected to be signatures of physical phenomena of interest, or exploration targeting the discovery of new behaviors (i.e., curiosity learning).

Here, we use the combined power of the BO and feedforward neural networks in the form of deep kernel learning (DKL) to enable the autonomous physical discovery in STEM-EELS of nanoplasmonic structures. We develop the associated workflow, quantify its performance on pre-acquired data of plasmonic nanoparticles, and deploy it on the operational microscope without any additional hardware to discover the edge plasmon functionality in  $\text{MnPS}_3$ ,<sup>36–39</sup> a relatively unexplored beam-sensitive 2D antiferromagnet.

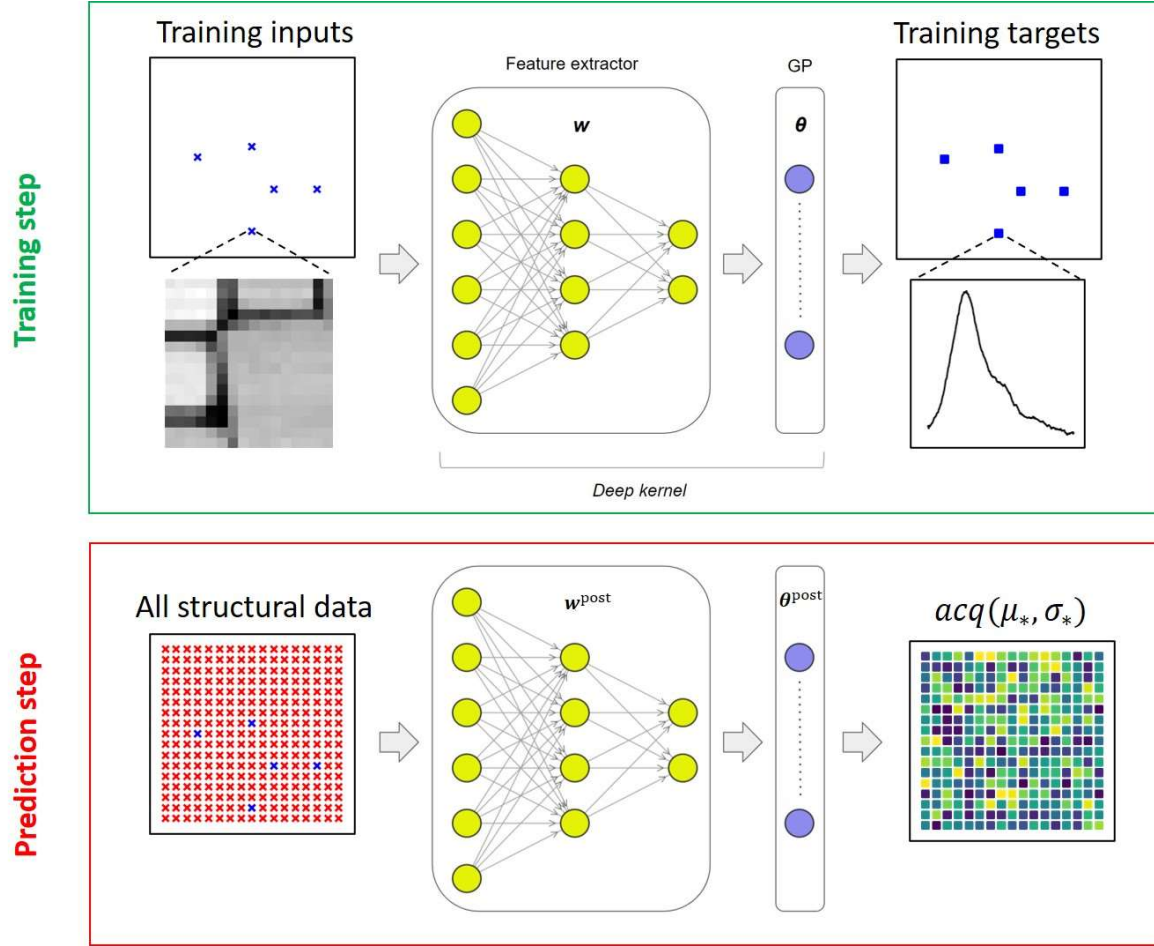


**Figure 1.** Schematic illustration of a single deep kernel learning (DKL) step for active learning of system properties where an input is a structural image, and an output is either a spectrum or a specific scalar property derived from it. Computationally wise, a feedforward neural network takes structural images and embeds them into a low-dimensional feature space in which a standard (‘base’) Gaussian process kernel operates. At training step, the weights ( $\mathbf{w}$ ) of the neural network and the hyperparameters ( $\boldsymbol{\theta}$ ) of the base kernel are optimized jointly using a small number of available measurements. Once a DKL model is trained, it can be used to compute expected function value ( $\mu_*$ ) and the associated uncertainty ( $\sigma_*$ ) for all structural data (for which there are no measured spectra). These are used to derive the acquisition function,  $acq(\mu_*, \sigma_*)$ , for selecting the next measurement point according to  $x_{\text{next}} = \text{argmax}(acq)$ .

As a model system, we have chosen fluorine and tin co-doped indium oxide nanoparticles whose plasmon response lies in the near infrared. This is the same material system studied in previous works<sup>40–44</sup> and we find it to be an excellent choice for visualizing the spatial dependence of a variety of plasmonic features that depend on geometry and local particle organization. The typical image and several spectra are shown in Figure 2. It is common to show deconvolved

components using exploratory data techniques such as non-negative matrix factorization (NMF) for visualizing the locality of the spectral behavior.<sup>45–48</sup> Here, we show the NMF in the supplementary materials and code which is available in the notebook, but we do not discuss it here. Figure 2 (A and B) largely illustrate the rich plasmonic features possible in this system.

A crucial aspect of NMF and other spectrum-based linear and manifold learning methods is that they do not consider any relationships to the structural data or the spatial location from which the spectra are acquired. However, it is these relationships which guides the human operator to decide where to perform measurements. Previously, we have introduced the *im2spec* approach,<sup>43,49</sup> using the encoder-decoder neural network architecture to establish the correlative relationship between local structure and functional responses. However, the *im2spec* approach requires a full data set to perform the analysis. Furthermore, transferring a pretrained deterministic neural network to autonomous experiment is limited both by out-of-distribution effects and the capability of the network to “discover” only the phenomena it has been trained on. In the machine learning (ML) community, the A/B testing type algorithms are known to be least data efficient and most sensitive to the changes in the data generation process.

With this in mind, and using the same dataset, we illustrate the deep kernel learning approach, where the fully available structural data is used to actively navigate the spectrum “acquisition” process. Similar to the *im2spec* method, we split the structural image into a set of patches of size  $w$  at every spatial coordinate and pair these with the EEL spectrum at that coordinate. The patches are hence the structural descriptors, whereas EEL spectra are the target functionalities (see Figure 1). Here, we assume that the structural information is available everywhere, whereas spectra are available only for a fraction of locations. Figure 2 C-F illustrates the patch formation and corresponding spectra.

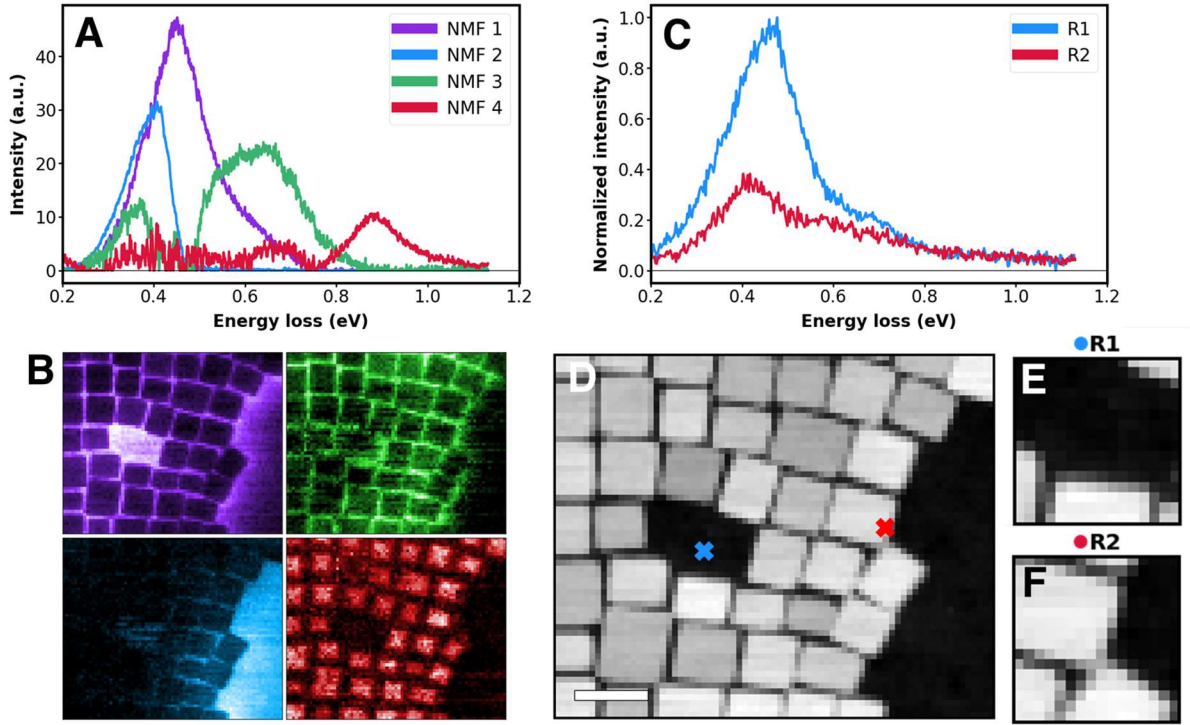


**Figure 2.** System overview and interpretation of data by processing techniques. NMF deconvolution for  $N = 4$  components where spectral endmembers and abundance maps are shown in A and B, respectively. Sub-image formation from structural image in D is shown in E and F, where EEL spectra in C correspond to response from center pixel in sub-images E and F. The data set of the plasmonic cubes is used from [42,43].

To illustrate the behavior of DKL in this system, we first demonstrate its potential to reconstruct the data for full sampling, followed by sparse sampling. In the latter case, we assume that we have access to the full structural information within the image and the EEL spectra at several locations. We postulate the existence of a (unknown) relationship between local structure and EEL spectrum and seek to reconstruct it for the full data set. However, here we assume that only partial information on functionality is available.

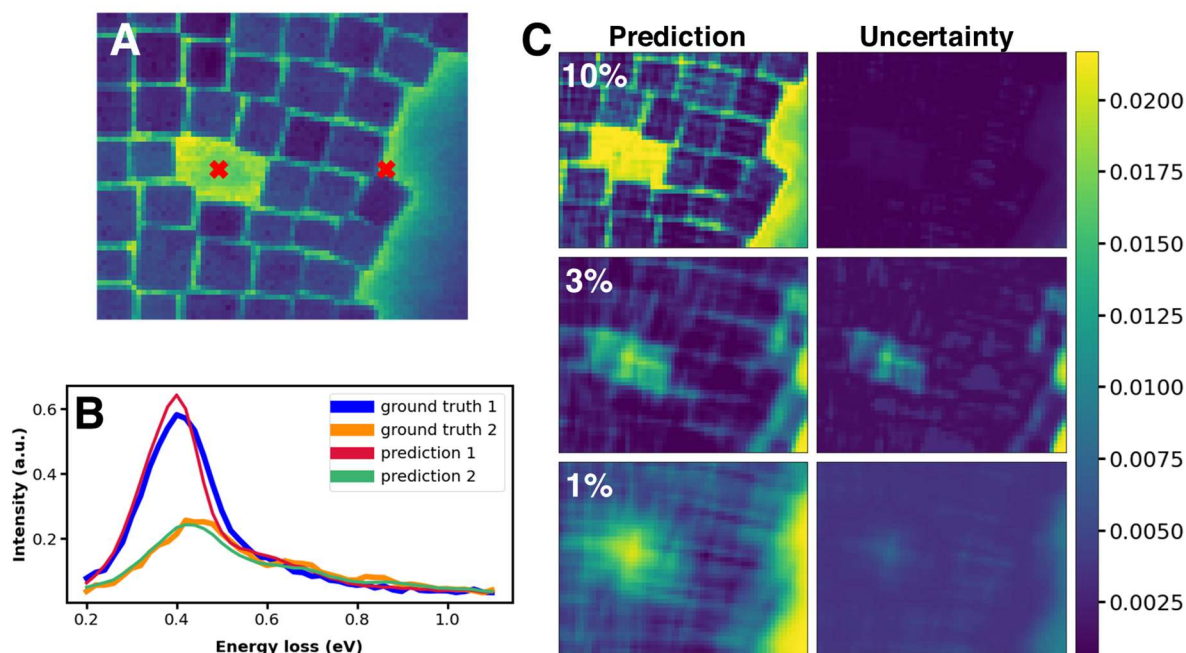


**Figure 3.** DKL model performance for full data reconstruction. (A) Ground truth image representing energy average over all energies, with selected ground truth spectra and DKL spectral predictions using all data shown in (B). DKL predictions and associated uncertainties using partial data (indicated by percentages) are shown in (C). Color scale is for uncertainties only.

The DKL reconstruction of structure-property relationships for random selection of sampling points is shown in Figure 3. Individual spectral reconstruction using all known points for selected coordinates in A is shown in B, which are compared to the ground truth spectra. We note that the DKL reconstructs the spectra from images. However, for visualization purposes we further calculate the energy-averaged images across the entire spectrum, which are shown in Figure 3 C for 10%, 3%, and 1% fraction of known points, where the corresponding uncertainties in the spectral reconstructions are also shown. Even for only 1% known points, the reconstruction is strikingly good, indicating that utilizing structural similarity allows to harness wealth of information contained in the structure-spectra relationships.

To rationalize these observations, we note that there is a relationship between local structures and EEL spectra. Generally, it can be expected that similar structures have similar spectra and discovering the relationship between the two constitutes the correlative model. The deviations from such relationships signify the presence of unknown mechanisms, with the uncertainty maps providing likely spatial locations on where they manifest. However, the points in this case are chosen randomly (i.e., absent any knowledge of the system) and hence behaviors of interest localized in a small number of spatial locations remain poorly explored.



The analysis above illustrates the power of DKL to reconstruct spectra from structure based on partial data and yield corresponding uncertainties. However, the ultimate target of autonomous experiment is not only reconstruction of behaviors, but also the search for specific behaviors of interest. To understand fundamental principles behind this process, we note that each human-led experiment is guided by the combination of exploratory and exploitative strategies. Exploratory strategies generally target the discovery of possible behaviors in the system. In exploitative strategies, we seek to find new behaviors, refine the parameters of the known models, or refine a certain hypothesis.

The flexibility of the DKL allows exploration of the image space based on the combination of the predicted target function and its uncertainty, where both are vectors. This allows significant flexibility in defining exploration and exploitation strategies, based for example on the maximum value of a function, total integrated uncertainty, or other criteria. However, this also provides a unique opportunity to define physics-based acquisition functions that target the behaviors of interest as reflected in spectra. In other words, much like human-based exploration of data after acquisition, here we can formulate the exploration criterion based on the physical behavior of interest, whether it is specific peak intensity or width, peak intensity ratios, presence of certain features, similarity to previously known behaviors, etc.

Here, we first illustrate this approach on the pre-acquired data, with the full spectral data set (invisible to the DKL algorithm) being available as a ground truth. As a test case, after removing the zero-loss peak (ZLP) in the usual manner<sup>50,51</sup> by fitting a power law to the ZLP, we use the maximum spectral intensity is used as the optimization parameter for DKL. For the plasmonic nanoparticles under test, it turns out that the maximum intensity generally corresponds to a collective plasmon resonance which is most strongly observed when the electron probe is near - but not on - particles. By merely attempting to maximize spectral intensity, in this case, DKL can determine the relationship between intense spectral response and local geometries which partially contain particles. Figure 4 illustrates the discovery process at several different stages (number of measurement points). Strikingly, even at very few measured points, the model has learned the relationship between structure in the HAADF and maximizing plasmon intensity, as illustrated by the acquisition functions and model predictions in Figure 4 C.

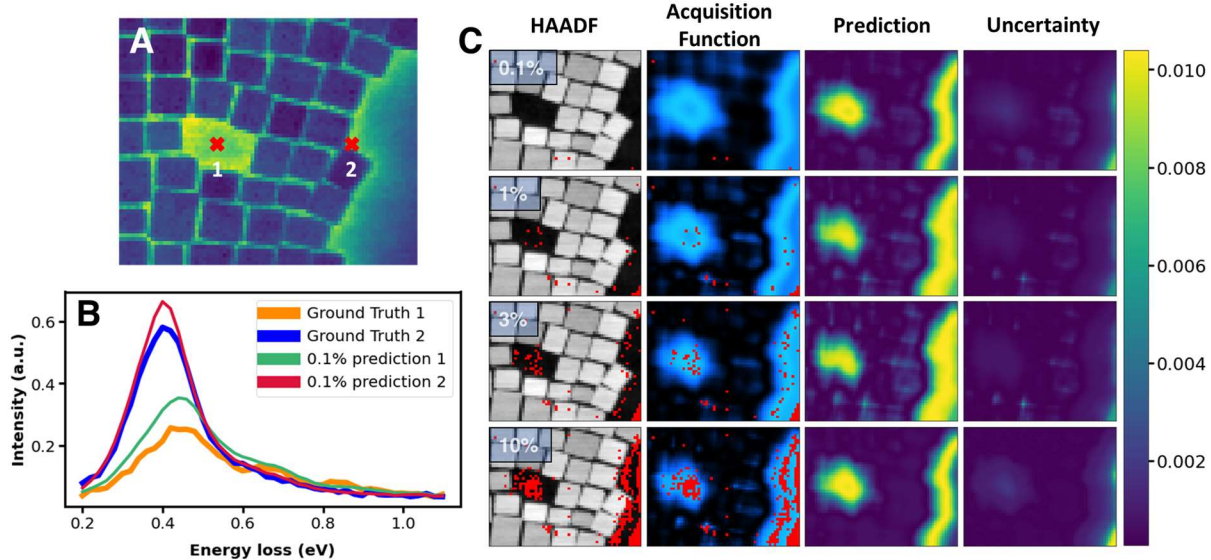


**Figure 4.** DKL discovery pathway for edge plasmon search. Spatially averaged plasmon spectrum is shown in A, where the model’s goal is to optimize the peak near 0.4 eV in (B). DKL pathway shown in panel (C) for increasing number of measured points; sampled points are shown in HAADF’s and (scalarized) acquisition functions in red, with DKL predictions and associated uncertainties also shown for where to best optimize maximization of the plasmon peak. Color scale is for uncertainties only.

Finally, we proceed to implement the DKL-based discovery in the autonomous experiment implemented on an operational Scanning Transmission Electron Microscope. Here, we used the NION Monochromated Aberration Corrected STEM (MACSTEM) and utilized the Python-scripting environment enabled by the SWIFT software suite<sup>52</sup> to establish the communication between DKL control routines and the beam position. A link between the EELS camera and SWIFT is already present since we use the NION IRIS spectrometer and camera system, therefore all data modalities (EELS, 4D-STEM, ADF) are accessible directly *via* a Python interface. Additional details are available in Materials and Methods section.

Here, we illustrate this approach for physics-driven discovery of plasmonic behavior discovery in  $\text{MnPS}_3$ , a less-known layered 2D van der Waals antiferromagnet. By analogy with other layered materials, we hypothesize that this material system should demonstrate specific plasmonic behaviors in the vicinity of interfaces, i.e., develop edge plasmons. The physical criterion for edge plasmon detection is the presence of the peak in EELS spectrum below the bulk plasmon. Hence, here we choose to optimize a peak ratio in the EEL spectrum where we posit the existence of a low energy electronic feature as well as a higher energy bulk plasmon resonance. The EEL spectra predicted from the structural descriptors are fit with two Lorentzian functions whose peak positions can fluctuate in energy but not overlap. The ratio of the amplitudes of the two are then used as the guiding principle in the autonomous experiment, where we seek to maximize the low energy feature and simultaneously minimize the bulk plasmon. Emphasis is placed on the fact that *a priori* we have no knowledge of any edge plasmon behavior in this material – we merely suggest a physical criterion in which we are interested. Equally important is

that this material is rather sensitive to electron beam irradiation, making high-fidelity hyperspectral imaging difficult. This lends well to the paradigm of autonomous experiment which allows to only irradiate regions that are deemed to be of interest, limiting the total dose the specimen receives.

The autonomous experiment (AE) utilizing the DKL workflow is illustrated in Figure 5, where a HAADF-STEM and selected EEL spectra of an exfoliated 2D flake consisting of several layers are shown. We first demonstrate in Figure 5C the DKL pathway, prediction, and acquisition function as a function of number of measured points when we choose to optimize the peak ratio previously discussed. Fairly quickly the DKL recognizes the relationship between the boundary of the flake and vacuum, in which a strong localized edge plasmon is found to exist and the higher energy bulk plasmon is weak or non-existent. Note that the top edge is more favorable than other edges presumably due to a sharper boundary. After measuring between 10 and 25 EEL spectra (which corresponds to only 1% of the entire space), it is apparent that the DKL predicts the location of edge modes rather well (Figure 5C, DKL Prediction). This has implication that after only a fraction of points are initially sampled, the model either need not be trained further or not as frequently, allowing a substantial speed increase.

Note that the choice of the physical model influences the discovery pathway and consequently the features that are discovered. Once again, this is similar to the human-based workflow, when depending on the specific hypothesis the operator will choose a different sequence of measurements. To illustrate this, we change the criterion from peak ratios to maximum peak intensity as is shown in Figure 5D. In this case, the maximum peak intensity appears to correspond to the bulk plasmon resonance, which generally increases in strength with thickness. As we would expect, since the intensity in the HAADF can be treated as a measurement of relative thickness (at these scales), we observe the DKL pathway to preponderantly explore the regions *on* the flake. This second search criterion serves to support the fact that this autonomous experiment enabled by DKL indeed does search for physics that depends on the built-in models that are provided. In the supplementary information, videos are provided which show the algorithm in action with more detail.

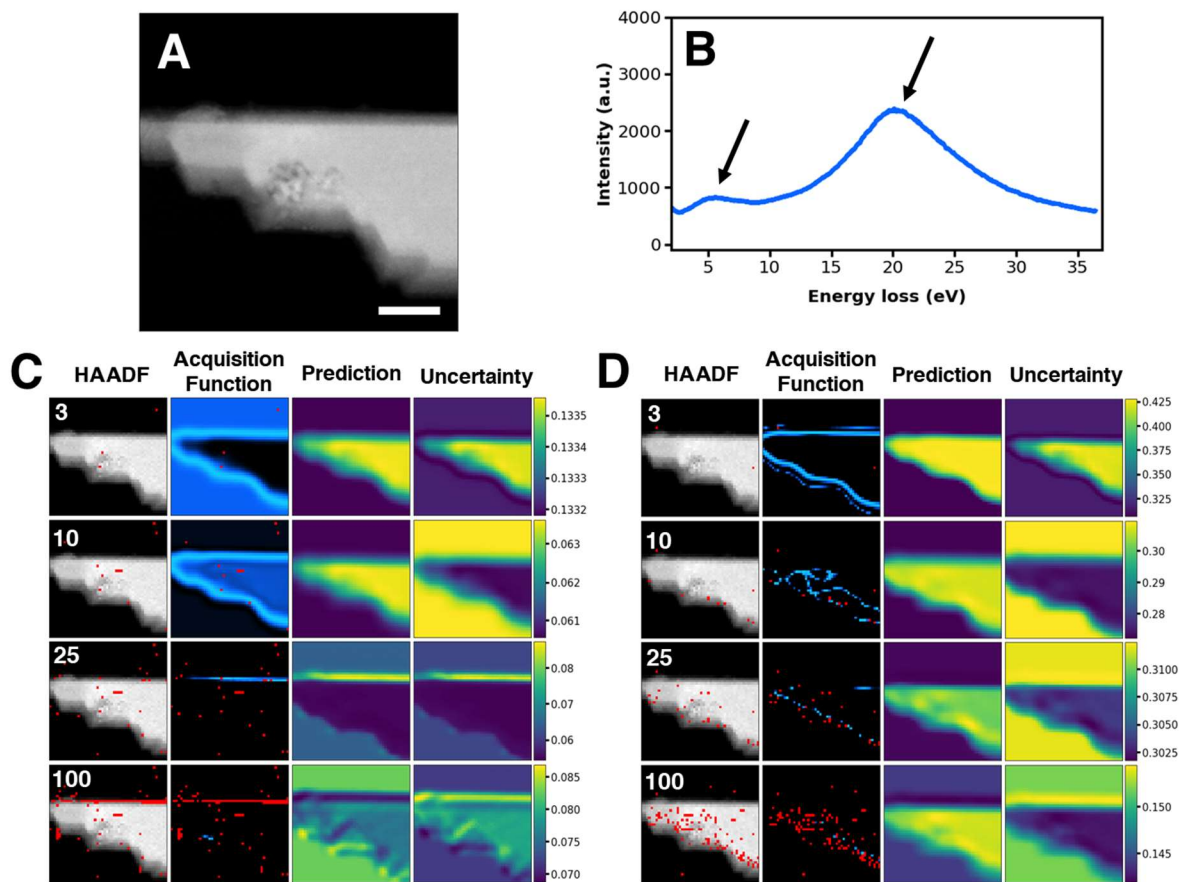


**Figure 5.** Autonomous experimentation (AE) enabled by DKL. Autonomous experiment with structural (HAADF) image of 2D section of suspended  $\text{MnPS}_3$  shown in (A); autonomous peak ratio optimization shown in (C), while autonomous optimization of maximum spectral intensity shown in (D). Average spectrum from all visited points in autonomous experiment in (C) is shown in (B,) where arrows indicate the peaks from which a peak ratio is determined. Maximum spectral intensity in most space tends to relate to high energy peak near 20 eV. Process shown for 3, 10, 25, and 100 acquired measurements for two different physics search criteria employed: peak ratio optimization (C) and maximization of spectral intensity (D). Scalebar in (A) 50 nm.

To summarize, we have implemented the physics discovery workflow for electron energy loss spectroscopy in scanning transmission electron microscopy. This approach uses the structural information as initial data for scientific discovery and uses active learning to build the structure-property relationships in the system under investigation. The discovery process is guided by the physics-based acquisition function that allows incorporation of physical models, target functionalities, or discovery of novel phenomena. Here, this approach enabled the detection and realization of edge plasmon behavior in the 2D layered antiferromagnet  $\text{MnPS}_3$ . No prior knowledge of edge plasmon activity has been mentioned in literature or was expected to occur. Nonetheless, armed with active learning provided by the DKL as well as some basic physics

instructions, a new functionality in this material was discovered that in fact may prove to be useful in quantum and nanophotonic technologies.

A key point about the DKL discovery is that almost any physical criteria can be put forth – this may be as simple or as complicated as desired. In STEM, the autonomous experimentation can be readily extended beyond the spectral measurements such as EELS and EDS, towards 4D-STEM modes. Here, scalar-derived quantities such as lattice parameters, strain, and electric fields that are calculated from a diffraction pattern, along with their uncertainties, can be used as a part of the exploration criteria. With the myriad of different modalities that are possible in the electron microscope and other probe-based imaging such as variants of Scanning Probe Microscopy, DKL holds the key to opening the floodgates of autonomous experimentation.

Perhaps even more importantly, similar principles (sequential scanning of feature rich parameter spaces) underpin multiple other areas of scientific discovery, from instrumental characterization methods to the discovery of new materials, molecules, etc. We believe that the proposed principle combining the correlative ML prediction of complex responses combined with physics-based navigation can be of interest for multiple other areas.

**Acknowledgement:** This effort (electron microscopy, feature extraction) is based upon work supported by the U.S. Department of Energy (DOE), Office of Science, Basic Energy Sciences (BES), Materials Sciences and Engineering Division (K.M.R., S.V.K.) and was performed and partially supported (M.Z.) at the Oak Ridge National Laboratory's Center for Nanophase Materials Sciences (CNMS), a U.S. Department of Energy, Office of Science User Facility. The authors acknowledge Shin-Hum Cho and Delia J. Milliron for supplying semiconducting nanoparticles as well as Nan Huang and David G. Mandrus for the MnPS<sub>3</sub> used in this work.

## Materials and methods

### Materials

F,Sn:In<sub>2</sub>O<sub>3</sub> nanoparticles were chemically synthesized by Shin-Hum Cho and Delia J. Milliron using standard Schlenk line techniques with a modification of previously reported methods for continuous slow injection synthesis of indium oxide nanoparticles as described in [41].

MnPS<sub>3</sub> crystals were grown by Nan Huang and David G. Mandrus using a chemical vapor transport (CVT) method as described in [53]. Single crystals were mechanically exfoliated directly onto Au Quantifoil TEM grids.

### Autonomous Microscopy

As part of the NION Swift package, direct access *via* a Python scripting interface exists to both monitor and control various aspects of the NION MACSTEM. In our case, the electron probe position, EELS camera, and Ronchigram camera are all accessible with appropriate commands. This implies there is no additional hardware requirement for autonomous experiments using the NION systems. Installation of various required Python packages (e.g., PyTorch, SciPy, etc.) was done such that the model training is performed on the microscope hardware PC. The CPU or GPU can be used for training, where in the form of scalar DKL and small/sparse data, use of a GPU presents no significant benefit. For vector DKL (i.e., full spectrum prediction), use of GPU is practically required due to needed parallelization of many spectral targets.

Autonomous experiment begins with the collection of HAADF-STEM (structural) image of size  $m \times n$  pixels, followed by  $N$  number of randomly sampled EEL spectra in the same space, where here  $m \times n$  is 50 x 50 and  $N$  is usually two or three. The probe is then immediately moved to a pre-defined safe location (e.g., for beam sensitive samples) or is blanked. Image patches (features) are created for all pixels in the HAADF using a user-specified window size, e.g., 8 x 8 pixels, which should be appropriately selected based on field of view and structural details that may be contained in each image patch.

Searching for particular physical effects is facilitated by specification of search criteria – in scalar DKL, the EEL spectrum is reduced to a single scalar quantity in any imaginable way. Note that in vector DKL, the entire spectrum does not need to be reduced to a scalar quantity, though depending on GPU, the number of spectral channels may be limited. In this work, we showed examples of two relatively simple criteria with scalar DKL– maximum spectral intensity and a peak ratio of fitted curves. Curve fitting is performed by defining a Lorentzian function and using the SciPy package in Python.

The DKL model is trained with each additional EELS measurement such that it continuously learns structure-property relationships. This is adjustable to the point where training may be halted at a certain number of measurements, or a pre-trained model may be used, however the use of pre-trained models is not discussed here as our focus is that of *active* learning. A built-in

exploration parameter also exists in the model which allows for the balance of exploitation and exploration of the data space, i.e., this might help to avoid remaining in a local minimum.

## Gaussian Process Regression and Bayesian Optimization

In the Gaussian process regression setting, given inputs  $X = (x_1, \dots, x_N)$  and targets  $\mathbf{y} = (y_1, \dots, y_N)$ , we assume that each target point is generated according to<sup>54</sup>

$$y_n = f(x_n) + \varepsilon_n, \quad (1)$$

where  $f$  is drawn from a Gaussian process (GP) prior,  $f \sim \mathcal{GP}(0, k)$ , and  $\varepsilon_i \sim \mathcal{N}(0, s_n^2)$ . The covariance (kernel) function  $k$  defines a strength of correlation between points in the input space and its hyperparameters are learned from the data (along with the noise variance) by performing a gradient ascent on the log marginal likelihood. The most common choice of kernel is a radial basis function (RBF) which on one hand supports a large class of functions with various shapes but on the other hand have inductive biases toward very simple solutions.

Once a GP model is trained (i.e., the kernel and noise variance are learned), it can be used to compute predictive mean ( $\mu_*$ ) and variance ( $\Sigma_*$ ) for a new (test) point  $x_*$  as

$$\mu_* = \mathbf{k}_*^T (K + s_n^2 I)^{-1} \mathbf{y}, \quad (2a)$$

$$\Sigma_* = k(\mathbf{x}_*, \mathbf{x}_*) - \mathbf{k}_*^T (K + s_n^2 I)^{-1} \mathbf{k}_* \quad (2b)$$

where  $K$  is the  $n$ -by- $n$  matrix of covariances computed for all pairs of training points and  $\mathbf{k}_*$  is the vector of covariance between the test and training points. In the context of microscopy/spectroscopy, the training data ( $X$  and  $\mathbf{y}$ ) correspond to sparse measurements over a selected field of view (FOV) defined on rectangular grid of size  $i \times j$  whereas the new/test points ( $X_*$ ) correspond to yet unmeasured regions from the same FOV. The goal of Bayesian optimization (BO) is to discover regions where a particular functionality or structure is maximized using a minimal number of measurements. The next measurement points are selected using the maxima of so-called acquisition function(s) derived from the GP-predicted mean,  $\mu_*$ , and uncertainty,  $\sigma_* = \text{diag}(\Sigma_*)$  on the test data. The popular choice of acquisition functions is the expected improvement (EI), which tells a likelihood of the highest improvement over the current “best measurement”<sup>55</sup> and is defined as

$$\alpha_{\text{EI}} = (\mu(\mathbf{x}) - y^+ - \xi) \Phi\left(\frac{\mu(\mathbf{x}) - y^+ - \xi}{\sigma(\mathbf{x})}\right) + \sigma(\mathbf{x}) \phi\left(\frac{\mu(\mathbf{x}) - y^+ - \xi}{\sigma(\mathbf{x})}\right) \quad (3)$$

Unfortunately, the classical GP has several major limitations that preclude its widespread adoption for real-time microscopy and spectroscopy measurements. First, it does not scale well to high-dimensional ( $D \gtrsim 3$ ) inputs making it unsuitable for hyperspectral measurements ( $D \geq 3$ ) in online settings. Second, the classical GP does not actually learn the representations from the data. As such, it does not allow for using information obtained through different experimental modalities

for more efficient navigation during the BO. For example, it is not uncommon to see the associations between features observed in easy-to-acquire structural 2D images and those seen in spectroscopic data (the existence and strength of such associations depend on the particular system and experimental method), but it is not possible to exploit such associations in the BO setting with the classical GP approach.

## Deep Kernel Learning

One of the solutions to the aforementioned limitations of the classical GP is to combine a deep neural network with a Gaussian process. The former is well-known to be a powerful deterministic tool for representation learning that can easily scale to high-dimensional inputs whereas the latter provides the reliable uncertainty estimates. This hybrid solution is known as deep kernel learning (DKL)<sup>56</sup> which we schematically illustrated in Fig 1. Its central idea is straightforward. The high-dimensional input data is embedded by a feed-forward neural network  $g_\omega$  into the (latent) feature space where a standard (“base”) GP kernel operates. The new effective kernel is expressed as  $k_{DKL}(x, x') = k(g_\omega(x), g_\omega(x'))$ , where  $\omega$  are the parameters (weights and biases) of the neural network. The parameters of the base kernel and the weights of the neural network are trained jointly by maximizing the log marginal likelihood. Once trained, the DKL-GP model can make a prediction with quantified uncertainty on new (high-dimensional) input data for selecting the next measurement point according to Eq (2)-(3).

In the DKL GP, the inputs can be image patches extracted at  $(k, l)$  locations of the 2D grid and the targets can be either full spectra in those locations or some specific characteristic(s) of spectra such as intensity of selected peaks (note that the dimensionality of each input patch is equal to the total number of pixels contained in the patch; hence, even for a patch of  $8 \times 8$  the input dimensionality is 64). In this case, the DKL GP will learn a correlative structure-property relationship whereas the uncertainty in property prediction from patches of structural data at  $(k, l)$  points on the grid can be used for selecting the next measurement point using a pre-defined acquisition function. We note that while predicting property from structure can be also done with the *im2spec* type of encoder-decoder networks,<sup>43,49</sup> it does not output predictive uncertainty and hence cannot be used for the BO-based autonomous experimentation.

We note that during the exact GP training, the entire dataset must be passed “through” a model at once, which may not be possible for modern neural network architectures containing millions and sometimes billions of parameters even when using state-of-art Graphics Processing Units (GPUs). One possible solution is to use a stochastic variational (i.e., approximate) inference that allows for mini-batching of training data. At the same time, we found that in many cases the experimental observations can be well modeled by simple few-layer perceptrons (MLPs) with a much smaller number of parameters that can accommodate an entire dataset allowing for the exact GP training and inference. We also note that it is possible to use a neural network (pre-)trained in the offline setting (e.g., using the previously collected data) and “freeze” its weights during the



DKL training on new data from a similar experiment, which could save computational time/cost in the online setting.

### **Data availability**

The data used for analysis as well as additional materials are available through the Jupyter notebook located at: <https://github.com/kevinroccapriore/AE-DKL/>

## References

1. Pennycook, S. J. The impact of STEM aberration correction on materials science. *Ultramicroscopy* **180**, 22–33 (2017).
2. Gerber, C. & Lang, H. P. How the doors to the nanoworld were opened. *Nature Nanotech* **1**, 3–5 (2006).
3. Pennycook, S. J. Seeing the atoms more clearly: STEM imaging from the Crewe era to today. *Ultramicroscopy* **123**, 28–37 (2012).
4. Chisholm, M. F., Luo, W., Oxley, M. P., Pantelides, S. T. & Lee, H. N. Atomic-Scale Compensation Phenomena at Polar Interfaces. *Phys. Rev. Lett.* **105**, 197602 (2010).
5. Jia, C.-L. *et al.* Unit-cell scale mapping of ferroelectricity and tetragonality in epitaxial ultrathin ferroelectric films. *Nature Materials* **6**, 64–69 (2007).
6. Dai, Z., Slough, C. G. & Coleman, R. V. Charge-density-wave structure in NbSe<sub>3</sub> determined by scanning tunneling microscopy. *Phys. Rev. Lett.* **66**, 1318–1321 (1991).
7. Tsen, A. W. *et al.* Structure and control of charge density waves in two-dimensional 1T-TaS<sub>2</sub>. *PNAS* **112**, 15054–15059 (2015).
8. Roushan, P. *et al.* Topological surface states protected from backscattering by chiral spin texture. *Nature* **460**, 1106–1109 (2009).
9. Moler, K. A. Imaging quantum materials. *Nature Mater* **16**, 1049–1052 (2017).
10. Idrobo, J. C. *et al.* Temperature Measurement by a Nanoscale Electron Probe Using Energy Gain and Loss Spectroscopy. *Phys. Rev. Lett.* **120**, 095901 (2018).
11. Venkatraman, K., Levin, B. D. A., March, K., Rez, P. & Crozier, P. A. Vibrational spectroscopy at atomic resolution with electron impact scattering. *Nature Physics* **15**, 1237–1241 (2019).
12. Hage, F. S., Radtke, G., Kepaptsoglou, D. M., Lazzeri, M. & Ramasse, Q. M. Single-atom vibrational spectroscopy in the scanning transmission electron microscope. *Science* **367**, 1124–1127 (2020).
13. Krivanek, O. L. *et al.* Vibrational spectroscopy in the electron microscope. *Nature* **514**, 209–212 (2014).
14. Grillo, V. *et al.* Generation of Nondiffracting Electron Bessel Beams. *Phys. Rev. X* **4**, 011013 (2014).
15. Zachman, M. J., Tu, Z., Choudhury, S., Archer, L. A. & Kourkoutis, L. F. Cryo-STEM mapping of solid–liquid interfaces and dendrites in lithium-metal batteries. *Nature* **560**, 345–349 (2018).
16. Lagos, M. J., Trügler, A., Hohenester, U. & Batson, P. E. Mapping vibrational surface and bulk modes in a single nanocube. *Nature* **543**, 529–532 (2017).

17. Yin, P. & Radovanovic, P. V. Magnetoplasmon Resonances in Semiconductor Nanocrystals: Potential for a New Information Technology Platform. *ChemSusChem* **13**, 4885–4893 (2020).
18. Kociak, M., Henrard, L., Stéphan, O., Suenaga, K. & Colliex, C. Plasmons in layered nanospheres and nanotubes investigated by spatially resolved electron energy-loss spectroscopy. *Phys. Rev. B* **61**, 13936–13944 (2000).
19. Bigelow, N. W., Vaschillo, A., Iberi, V., Camden, J. P. & Masiello, D. J. Characterization of the Electron- and Photon-Driven Plasmonic Excitations of Metal Nanorods. *ACS Nano* **6**, 7497–7504 (2012).
20. Cherqui, C., Bigelow, N. W., Vaschillo, A., Goldwyn, H. & Masiello, D. J. Combined Tight-Binding and Numerical Electrodynamics Understanding of the STEM/EELS Magneto-optical Responses of Aromatic Plasmon-Supporting Metal Oligomers. *ACS Photonics* **1**, 1013–1024 (2014).
21. Nelayah, J. *et al.* Mapping surface plasmons on a single metallic nanoparticle. *Nature Physics* **3**, 348–353 (2007).
22. Zhou, W. *et al.* Atomically localized plasmon enhancement in monolayer graphene. *Nature Nanotech* **7**, 161–165 (2012).
23. Vasilevsky, N. A., Minnier, J., Haendel, M. A. & Champieux, R. E. Reproducible and reusable research: are journal data sharing policies meeting the mark? *PeerJ* **5**, e3208 (2017).
24. Blaiszik, B. *et al.* The Materials Data Facility: Data Services to Advance Materials Science Research. *JOM* **68**, 2045–2052 (2016).
25. Kalinin, S. V. *et al.* Automated and Autonomous Experiments in Electron and Scanning Probe Microscopy. *ACS Nano* (2021) doi:10.1021/acsnano.1c02104.
26. Dyck, O., Jesse, S. & Kalinin, S. V. A self-driving microscope and the Atomic Forge. *MRS Bulletin* **44**, 669–670 (2019).
27. Kelley, K. P. *et al.* Dynamic Manipulation in Piezoresponse Force Microscopy: Creating Nonequilibrium Phases with Large Electromechanical Response. *ACS Nano* **14**, 10569–10577 (2020).
28. Krull, A., Hirsch, P., Rother, C., Schiffrin, A. & Krull, C. Artificial-intelligence-driven scanning probe microscopy. *Commun Phys* **3**, 1–8 (2020).
29. Doty, C. *et al.* Design of a Graphical User Interface for Few-Shot Machine Learning Classification of Electron Microscopy Data. *arXiv:2107.10387 [cond-mat]* (2021).
30. Trentino, A. *et al.* Atomic-Level Structural Engineering of Graphene on a Mesoscopic Scale. *Nano Lett.* **21**, 5179–5185 (2021).
31. Sotres, J., Boyd, H. & Gonzalez-Martinez, J. F. Enabling autonomous scanning probe microscopy imaging of single molecules with deep learning. *Nanoscale* **13**, 9193–9203 (2021).

32. Jasper Snoek *et al.* Scalable Bayesian Optimization Using Deep Neural Networks. in *Proceedings of the 32nd International Conference on Machine Learning* (eds. Francis Bach & David Blei) vol. 37 2171–2180 (PMLR, 2015).
33. Noack, M. M. *et al.* Autonomous materials discovery driven by Gaussian process regression with inhomogeneous measurement noise and anisotropic kernels. *Sci Rep* **10**, 17663 (2020).
34. Noack, M. M. *et al.* Gaussian processes for autonomous data acquisition at large-scale synchrotron and neutron facilities. *Nat Rev Phys* 1–13 (2021) doi:10.1038/s42254-021-00345-y.
35. Vasudevan, R. K. *et al.* Autonomous Experiments in Scanning Probe Microscopy and Spectroscopy: Choosing Where to Explore Polarization Dynamics in Ferroelectrics. *ACS Nano* **15**, 11253–11262 (2021).
36. Susner, M. A., Chyasnachyus, M., McGuire, M. A., Ganesh, P. & Maksymovych, P. Metal Thio- and Selenophosphates as Multifunctional van der Waals Layered Materials. *Advanced Materials* **29**, 1602852 (2017).
37. Kumar, R., Jenjeti, R. N., Austeria, M. P. & Sampath, S. Bulk and few-layer MnPS<sub>3</sub>: a new candidate for field effect transistors and UV photodetectors. *J. Mater. Chem. C* **7**, 324–329 (2019).
38. Long, G. *et al.* Persistence of Magnetism in Atomically Thin MnPS<sub>3</sub> Crystals. *Nano Lett.* **20**, 2452–2459 (2020).
39. Neal, S. N. *et al.* Symmetry crossover in layered MPS<sub>3</sub> complexes (M={Mn}, {Fe}, {Ni}) via near-field infrared spectroscopy. *Phys. Rev. B* **102**, 085408 (2020).
40. Cho, S. H. *et al.* Syntheses of Colloidal F:In<sub>2</sub>O<sub>3</sub> Cubes: Fluorine-Induced Faceting and Infrared Plasmonic Response. *Chem. Mater.* **31**, 2661–2676 (2019).
41. Cho, S. H. *et al.* Spectrally tunable infrared plasmonic F,Sn:In<sub>2</sub>O<sub>3</sub> nanocrystal cubes. *J. Chem. Phys.* **152**, 014709 (2020).
42. Kalinin, S. V. *et al.* Separating Physically Distinct Mechanisms in Complex Infrared Plasmonic Nanostructures via Machine Learning Enhanced Electron Energy Loss Spectroscopy. *Advanced Optical Materials* 2001808 doi:<https://doi.org/10.1002/adom.202001808>.
43. Roccapiore, K. M., Ziatdinov, M., Cho, S. H., Hachtel, J. A. & Kalinin, S. V. Predictability of Localized Plasmonic Responses in Nanoparticle Assemblies. *Small* **17**, 2100181 (2021).
44. Roccapiore, K. M., Cho, S.-H., Lupini, A. R., Milliron, D. J. & Kalinin, S. V. Sculpting the plasmonic responses of nanoparticles by directed electron beam irradiation. *arXiv:2104.02165 [cond-mat, physics:physics]* (2021).
45. Shiga, M. *et al.* Sparse modeling of EELS and EDX spectral imaging data by nonnegative matrix factorization. *Ultramicroscopy* **170**, 43–59 (2016).

46. Zhang, S. & Scheu, C. Evaluation of EELS spectrum imaging data by spectral components and factors from multivariate analysis. *Microscopy* **67**, i133–i141 (2018).
47. Agrawal, A. *et al.* Resonant Coupling between Molecular Vibrations and Localized Surface Plasmon Resonance of Faceted Metal Oxide Nanocrystals. *Nano Lett.* **17**, 2611–2620 (2017).
48. Barrow, S. J. *et al.* Electron Energy Loss Spectroscopy Investigation into Symmetry in Gold Trimer and Tetramer Plasmonic Nanoparticle Structures. *ACS Nano* **10**, 8552–8563 (2016).
49. Kalinin, S. V., Kelley, K., Vasudevan, R. K. & Ziatdinov, M. Toward Decoding the Relationship between Domain Structure and Functionality in Ferroelectrics via Hidden Latent Variables. *ACS Appl. Mater. Interfaces* **13**, 1693–1703 (2021).
50. Kimoto, K., Ishizuka, K. & Matsui, Y. Decisive factors for realizing atomic-column resolution using STEM and EELS. *Micron* **39**, 257–262 (2008).
51. Hachtel, J. A., Lupini, A. R. & Idrobo, J. C. Exploring the capabilities of monochromated electron energy loss spectroscopy in the infrared regime. *Scientific Reports* **8**, 5637 (2018).
52. Meyer, C. *et al.* Nion Swift: Open Source Image Processing Software for Instrument Control, Data Acquisition, Organization, Visualization, and Analysis Using Python. *Microscopy and Microanalysis* **25**, 122–123 (2019).
53. Nitsche, R. & Wild, P. Crystal growth of metal-phosphorus-sulfur compounds by vapor transport. *Materials Research Bulletin* **5**, 419–423 (1970).
54. Rasmussen, C. E. & Williams, C. K. I. Gaussian Processes for Machine Learning (Adaptive Computation and Machine Learning). *The MIT Press* (2005).
55. Shahriari, B., Swersky, K., Wang, Z., Adams, R. P. & de Freitas, N. Taking the Human Out of the Loop: A Review of Bayesian Optimization. *Proceedings of the IEEE* **104**, 148–175 (2016).
56. Wilson, A. G., Hu, Z., Salakhutdinov, R. & Xing, E. P. Deep Kernel Learning. in *Artificial Intelligence and Statistics* 370–378 (PMLR, 2016).